

Observation of the Anderson metal-insulator transition with atomic matter waves: Theory and experiment

Gabriel Lemarié,¹ Julien Chabé,^{2,*} Pascal Szriftgiser,² Jean Claude Garreau,² Benoît Grémaud,^{1,3} and Dominique Delande¹

¹Laboratoire Kastler Brossel, UPMC-Paris 6, ENS, CNRS; 4 Place Jussieu, F-75005 Paris, France

²Laboratoire PhLAM, Université de Lille 1, CNRS, CERLA, F-59655 Villeneuve d'Ascq Cedex, France

³Centre for Quantum Technologies, National University of Singapore, 3 Science Drive 2, Singapore 117543, Singapore

(Received 20 July 2009; published 28 October 2009)

Using a cold atomic gas exposed to laser pulses—a realization of the chaotic quasiperiodic kicked rotor with three incommensurate frequencies—we study experimentally and theoretically the Anderson metal-insulator transition in three dimensions. Sensitive measurements of the atomic wave function and the use of finite-size scaling techniques make it possible to unambiguously demonstrate the existence of a quantum phase transition and to measure its critical exponents. By taking proper account of systematic corrections to one-parameter scaling, we show the universality of the critical exponent $\nu=1.59 \pm 0.01$, which is found to be equal to the one previously computed for the Anderson model.

DOI: [10.1103/PhysRevA.80.043626](https://doi.org/10.1103/PhysRevA.80.043626)

PACS number(s): 03.75.-b, 72.15.Rn, 64.70.Tg, 05.45.Mt

I. INTRODUCTION

The interplay between quantum effects and disorder is a subject actively studied for many decades, both theoretically and experimentally. It plays a particularly important role in condensed-matter physics, where, in a first approximation, a crystal is modeled as independent electrons interacting with a perfectly periodic lattice. The pioneering works of Bloch and Zener [1,2] showed however that most predictions based on this model are not verified in real crystals. For example, the Bloch theory predicts fully delocalized wave functions implying a ballistic transport of the electrons through the crystal. Moreover, in the presence of a constant bias potential, Zener predicted an oscillatory motion (the Bloch-Zener oscillations) due to quantum interference effects. This contradicts well-known experimental facts at least in usual conditions.

An obvious possible explanation of these contradictions is the fact that there are no perfect crystals. In a real crystal, some sites may be randomly occupied by ions of a different nature, thus, breaking the periodicity of the lattice. In 1958, Anderson considered this approach and postulated that the dominant effect of the disorder is to change randomly the on-site energy. Starting from this assumption, he constructed a simple model [3] of a single electron interacting with a lattice in the tight-binding approximation,

$$H_{\text{tb}} = \sum_{jn} \epsilon_{jn} |jn\rangle \langle jn| + \sum_{jn,k\mu} V_{jn,k\mu} |jn\rangle \langle k\mu|. \quad (1)$$

Here ϵ_{jn} are the energies associated with the states labeled by n at the sites j of the lattice, and the nondiagonal elements $V_{jn,k\mu}$ denote the matrix elements between these states. The diagonal part of the Hamiltonian corresponds to the potential energy and the nondiagonal part to the kinetic energy in a continuous space description. Disorder is introduced by giving the site energies ϵ_{jn} a *random* distribution. Anderson thus

showed that the electron wave functions can be *localized* by the disorder. This is naturally in sharp contrast with the prediction of the Bloch model.

The phenomenon of localization has its most striking manifestation in the transport properties of random media. If particle-particle interactions are negligible, exponentially localized states cannot contribute to transport at zero temperature since the coupling to phonons is negligible. Anderson localization as a consequence of the presence of disorder is one of the fundamental ingredients for the understanding of the existence of insulators and metals, and, in particular, the transition between the insulating and the metallic states of matter. An insulator is associated with localized states of the system, while a metal generally displays diffusive transport associated with delocalized states.

It was later shown that the three-dimensional (3D) Anderson model displayed a phase transition between a localized and a diffusive phase, the so-called Anderson metal-insulator transition. If the disorder is below a critical level, the localization disappears and one recovers a metallic (conductor) behavior [4]. The link between the disorder-induced metal-insulator transition and second-order phase transitions was established by reformulating the problem in terms of the renormalization group [5,6]. Based on Wegner's work and the ideas of Thouless and Landauer [5,7], it was possible to formulate the so-called *one-parameter scaling theory of localization* [8], one of the most fruitful approaches to the disorder-induced metal-insulator transition. The essential hypothesis of the scaling theory is that, close to the transition, a single relevant scaling variable describes the critical behavior.

An essential result of the one-parameter scaling theory is that the Anderson transition exists only in dimensions larger than two. In one dimension (1D), *all* electronic states are localized whatever *the* degree of randomness. In two dimensions, they are all localized, but only marginally, i.e., with a localization length exponentially large (thus possibly much larger than the sample size) for weak disorder.

In analogy to standard second-order phase transitions, the localization length ℓ is assumed to diverge at criticality according to a power law,

*Present address: Department of Physics, Ben-Gurion University, P.O. Box 653, Be'er Sheva IL-84105, Israel.

$$\ell \sim (W - W_c)^{-\nu}, \quad (2)$$

where ν as the localization length critical exponent, W is the disorder strength, and W_c as the critical disorder strength. The most important assumption of the theory, the one-parameter scaling hypothesis, was numerically validated using a finite-size scaling method developed in [9,10]. This technique, which implements a real-space renormalization, allowed to establish numerically the existence of a scaling function for the localization length. However, the critical exponents measured using this method $\nu \approx 1.57$ [11,12] were not compatible with the result $\nu=1$ obtained from a self-consistent approach of localization based on diagrammatic techniques, as developed in Ref. [13].

In the half-century since its birth, the Anderson model has become a paradigm for the studies of the interplay of quantum effects and disorder. Despite that, relatively few experimental results are available, for the following reasons: (i) it is experimentally hard to finely tune the disorder in a real crystal; (ii) the decoherence sources (collision with phonons, etc.) are difficult to master [14]; (iii) electrons in a crystal present strong mutual interactions [14,15], and (iv) the wave function of the electrons in the crystal is not directly accessible, only transport properties can be directly measured [16].

It is thus interesting to search for other systems that display the Anderson transition but are more favorable for experimental studies. Indeed, the concept of Anderson localization has progressively been extended from its original solid-state physics scope to a variety of systems, where a wave propagates in a disordered medium, for example, electromagnetic radiation [17,18] and sound waves [19–21]. Photons propagating in disordered materials revealed to be an excellent system to observe the effects of localization [17]. However, in such systems, there is always some absorption, whose signature can be quite similar to the signature of localization. Also, the measured quantity is the transmission, and the wave function itself is not accessible. The recent experimental observation of Anderson *localization* [22] using ultracold atomic matter waves has been done in a 1D situation, where states are always localized and no metal-insulator *transition* exists.

A very interesting Anderson-type system is obtained by combining the Anderson model with another paradigmatic system, the kicked rotor (KR), which has been theoretically studied for almost three decades. This system is well known to be classically chaotic [23], and chaos plays here the role of a “dynamical” disorder. In the quantum case, the KR displays a localization phenomenon called “dynamical localization” (DL) [24], which is analogous to the 1D-Anderson localization [25]. Moreover, a quasiperiodic generalization of the kicked rotor, substantially equivalent to the 3D Anderson model, was numerically shown to display an Anderson-like phase transition [26]. Experimental studies of the quantum kicked rotor were boosted by the realization of such a system with laser-cooled atoms interacting with a standing wave by Raizen and co-workers, who observed, for the first time, the Anderson localization with matter waves [27].

In the present paper, we describe in detail a realization of an atomic matter-wave system that allows us to observe the Anderson metal-insulator transition [28]. We report a full characterization of this phase transition, which includes an experimental validation of the one-parameter scaling hypothesis and the first nonambiguous experimental determination of the critical exponent ν . Last but not least, we show numerically that the quantum chaotic system we consider has the *same* critical behavior as the true random 3D Anderson model. In particular, we show that the two models belong to the same universality class. Section II introduces the cold-atom realization of the periodic (standard) KR and its equivalence with the 1D Anderson model, as well as the quasiperiodic generalization of this system that is equivalent of the 3D-Anderson model. Section III describes the corresponding experimental setup, paying attention to its experimental limits (decoherence, stray effects, and limited observation time). In Sec. IV we report our direct experimental observation of the metal-insulator transition. In Sec. V a scaling procedure is introduced that allows us to overcome experimental limitations and determine the critical exponent corresponding to the Anderson transition. Section VI is devoted to the universality of the critical behavior. Section VII concludes the paper.

II. ATOMIC KICKED ROTOR AND ITS RELATION TO THE ANDERSON MODEL

A. Atomic kicked rotor

Consider a two level atom interacting with a laser standing wave of frequency $\omega_L = k_L c$ detuned by $\Delta_L = \omega_L - \omega_0$ from the atomic transition of frequency ω_0 . It is well known that there are two kinds of interactions between the atom and the radiation. First, the atom can absorb a photon from the laser and re-emit it spontaneously in a random direction. This is a dissipative process giving rise to radiation pressure force, whose rate is $\Gamma \Omega^2 / 4\Delta_L^2$, where Γ is the natural width and Ω is the resonant Rabi frequency (we assume $|\Delta_L| \gg \Gamma$). Second, the atom can pick a photon in a laser mode and emit it in the same (or another) laser mode by stimulated emission. This conservative process is associated with a potential acting on the atom’s center-of-mass motion called the optical or dipole potential. For a standing wave, this potential is

$$V_{\text{opt}} = \frac{\hbar \Omega^2}{8\Delta_L} \cos(2k_L X), \quad (3)$$

where X is the atom center-of-mass position along the standing wave. Clearly, this interaction is one dimensional, as momentum exchanges between the atom and the radiation are always along the standing wave. The atom absorbs a photon in one of the propagating beams and emits it in the counter-propagating beam, leading to a quantized momentum exchange of $2\hbar k_L$ along the X axis. An important point is that the optical potential amplitude scales as Ω^2 / Δ_L , whereas the spontaneous emission rate scales as $\Gamma \Omega^2 / \Delta_L^2$. In the regime $|\Delta_L| \gg \Gamma$, the optical potential is the dominant contribution to the dynamics, with spontaneous emission events being rare. Moreover, one can reduce the spontaneous emission rate by

increasing the detuning Δ_L , provided that the laser has enough power to keep the potential amplitude at the required level.

Suppose now that, instead of having the atom interacting continuously with the standing wave, one modulates the radiation intensity periodically (with period T_1) so that it is on for a short time τ (as compared to the atom dynamics) and off the rest of the period. One then obtains the Hamiltonian

$$H = \frac{P^2}{2M} + \frac{\hbar\Omega^2\tau}{8\Delta_L} \cos(2k_L X) \sum_n \delta_\tau(t' - nT_1), \quad (4)$$

where $\delta_\tau(t) = 1/\tau$ if $|t| \leq \tau/2$ and zero otherwise. This functions tend to the Dirac δ function as $\tau \rightarrow 0$.

It is useful to introduce a set of scaled dimensionless units,

$$\begin{aligned} x &= 2k_L X, \\ p &= 2k_L T_1 P/M, \\ t &= t'/T_1, \\ K &= \frac{\hbar\Omega^2 T_1 \tau k_L^2}{2M\Delta_L}, \\ \bar{k} &= 4\hbar k_L^2 T_1/M, \\ \mathcal{H} &= \frac{4k_L^2 T_1^2}{M} H. \end{aligned} \quad (5)$$

In the limit of short pulses $\tau \ll T_1$, one then has

$$\mathcal{H} = \frac{p^2}{2} + K \cos x \sum_n \delta(t - n), \quad (6)$$

which is precisely the Hamiltonian of the kicked rotor [23,29]. One has thus realized an atomic kicked rotor [27]. The above Hamiltonian is associated with the Schrödinger equation

$$i\bar{k} \frac{\partial \psi}{\partial t} = \mathcal{H} \psi. \quad (7)$$

\bar{k} plays the crucial role of an effective Planck constant, which can be adjusted at will by modifying, e.g., the period T_1 . As shown in the following, the most interesting physics takes place in the momentum space. The scaling [Eqs. (5)] is such that $P = 2\hbar k_L$ corresponds to $p = \bar{k}$. If the atom is cold enough that its typical momentum is comparable to $2\hbar k_L$ (the “quantum” of momentum exchange), quantum effects can be observed in the system. Fortunately, magneto-optical traps (MOTs) produce atoms with a typical momentum of a few $\hbar k_L$. It is customary to measure the atomic momentum P in units of $2\hbar k_L$, i.e., measure p in units of \bar{k} . We thus will use

$$\mathfrak{p} = \frac{p}{\bar{k}} = \frac{P}{2\hbar k_L}. \quad (8)$$

For $K \geq 5$, the classical KR is fully chaotic, and the dynamics, although perfectly deterministic, behaves like a

pseudorandom diffusive process known as “chaotic diffusion.” For this reason, K is usually called “stochasticity parameter.” The existence of classical chaos can be seen by integrating the classical equations of motion corresponding to Eq. (6) over a period, which leads to the so-called “standard map”

$$x_{t+1} - x_t = p_{t+1}, \quad (9)$$

$$p_{t+1} - p_t = K \sin x_t. \quad (10)$$

If the stochasticity parameter K is large enough, $\sin x_t$ generates random numbers for successive t values. The momentum then performs a random (though deterministic) walk and the kinetic energy (averaged over the initial conditions) increases linearly with time. If—as we assume in the following—the initial state is a narrow momentum distribution centered around the origin $\mathfrak{p} = 0$, one obtains

$$\langle \mathfrak{p}^2 \rangle(t) = Dt, \quad (11)$$

with $D \approx K^2/2\bar{k}^2$ being the diffusion constant.

In the quantum case, a chaotic diffusion is observed for times shorter than a characteristic “localization time” $\tau_{\text{loc}} = D/2$, after which quantum interferences buildup in the system that eventually “freeze” the dynamics, suppressing the diffusion. The mean kinetic energy then tends to a constant $\langle \mathfrak{p}^2 \rangle(t \rightarrow \infty) \rightarrow 2\ell^2$ with $\ell \approx K^2/4\bar{k}^2$ [30]. At the same time, the momentum distribution changes from a Gaussian shape characteristic of a diffusive process to a localized exponential shape $\approx \exp(-|\mathfrak{p}|/\ell)$. This phenomenon is called dynamical localization (DL), meaning that the localization takes place in momentum space. In fact, as shown below, DL is intimately related to the Anderson localization, with, however, an important difference. DL takes place in *momentum* space, whereas Anderson localization is in *real* space.

B. Equivalence with the 1D-Anderson model

Let us consider the KR quantum dynamics. From a microscopic point of view, the motion is determined by the evolution operator over one period

$$U = e^{-iK \cos x/\bar{k}} e^{-ip^2/2\bar{k}}, \quad (12)$$

whose eigenstates form a basis set allowing to calculate the temporal evolution. These *Floquet states* $|\phi\rangle$ are fully characterized by their quasienergy ω , defined modulo 2π

$$U|\phi_\omega\rangle = e^{-i\omega}|\phi_\omega\rangle. \quad (13)$$

The Hamiltonian [Eq. (6)] is 2π periodic in position x , and so is the evolution operator [Eq. (12)]. The Bloch theorem tells us that a Floquet eigenstate is a product of a periodic function of x by a plane wave $\exp i\beta x$ with $0 \leq \beta < 1$, is a constant, $\beta\bar{k}$ being usually called the “quasimomentum.” A trivial transformation shows that one can equivalently consider periodic functions of x governed by the Hamiltonian [Eq. (6)], where p is replaced by $p + \beta\bar{k}$. In the following discussion, we will omit for simplicity the quasimomentum, although it is straightforward to take it into account. Note that in all numerical simulations shown hereafter, we per-

form an averaging over the quasimomentum, to follow the experimental conditions where an incoherent sum of all quasimomenta is prepared.

At this point, contact with a 1D Anderson tight-binding model can be made by reformulating Eq. (13) for the Floquet states [25]. First, we rewrite the (unitary) kick operator,

$$e^{-iK \cos x/\hbar} = \frac{1 + iW(x)}{1 - iW(x)}, \quad (14)$$

with

$$W(x) = \tan(K \cos x/2\hbar). \quad (15)$$

The periodic function $W(x)$ can be expanded in a Fourier series

$$W(x) = \sum_r W_r e^{irx}. \quad (16)$$

Similarly, for the kinetic part, one gets

$$e^{-i(p^2/2\hbar - \omega)} = \frac{1 + iV}{1 - iV}, \quad (17)$$

where V is diagonal in the momentum eigenbasis $|m\rangle \equiv |p = \hbar m\rangle$. Second, we make the following expansion in the momentum eigenbasis:

$$\frac{1}{1 - iW(x)} |\phi_\omega\rangle = \sum_m \Phi_m |m\rangle. \quad (18)$$

Then, the eigenequation for the Floquet state can be rewritten as

$$\epsilon_m \Phi_m + \sum_{r \neq 0} W_r \Phi_{m-r} = -W_0 \Phi_m, \quad (19)$$

with $\epsilon_m = \tan[\frac{1}{2}(\omega - m^2 \hbar/2)]$ [31].

This is the equation for a tight-binding model with hopping elements W_r to the r th neighbor, with eigenenergy W_0 , and with on-site energy ϵ_m . The hopping elements are not restricted to nearest neighbors, but they decrease exponentially with r [32]. In the original Anderson model, a random distribution is assigned to ϵ_m . Here, the sequence ϵ_m , although not satisfying the most stringent mathematical tests of randomness, is nevertheless pseudorandom. These two conditions are sufficient for the Anderson localization to take place. The hopping integrals W_r increase with the kick strength K , which thus plays the role of a control parameter in the Anderson model (19). Note that if \hbar is a rational multiple of 2π , the ϵ_m 's are periodic in m . This leads to the quantum resonances of the kicked rotor, where the states are extended.

When \hbar is incommensurate with 2π , the Floquet states are found to be exponentially localized, and this property accounts for dynamical localization. As shown in [33], the localization length observed at long times for a wave packet is essentially identical to the localization length of individual Floquet states.

Many references discuss the detailed correspondence between quantum behavior of this dynamical system and Anderson localization. In Ref. [29], an analogy between the

KR and band random matrices was pointed out; the latter has been reduced to a 1D nonlinear σ model [34] similar to those employed in the localization theory [35]. In Ref. [36], the direct correspondence between the KR and the diffusive supersymmetric nonlinear σ model was demonstrated. A diagrammatic approach [37] to the dynamical localization in the kicked Rotor was reported in [38].

C. Quasiperiodic kicked Rotor and its analogy to the 3D-Anderson model

As the Anderson transition exists only in three (or more) dimensions, one must generalize the KR to obtain a system analogous to a 3D Anderson model.

Different generalizations of the KR have been theoretically considered as analogs of the 3D-Anderson model [39,40]. Here we use the convenient three-incommensurate-frequencies generalization introduced in Refs. [26,41]

$$\mathcal{H}_{\text{qp}} = \frac{p^2}{2} + \mathcal{K}(t) \cos x \sum_n \delta(t-n), \quad (20)$$

obtained simply by modulating the amplitude of the standing-wave pulses with two new frequencies ω_2 and ω_3 ,

$$\mathcal{K}(t) = K[1 + \varepsilon \cos(\omega_2 t + \varphi_2) \cos(\omega_3 t + \varphi_3)]. \quad (21)$$

One can legitimately ask where is the three-dimensional aspect in the latter Hamiltonian? An answer can be given by drawing a formal analogy between the quasiperiodic kicked rotor and a 3D kicked rotor with an initial condition taken as “plane source” (see below).

We start from the Hamiltonian of a 3D periodically kicked rotor,

$$\mathcal{H} = \frac{p_1^2}{2} + \omega_2 p_2 + \omega_3 p_3 + K \cos x_1 [1 + \varepsilon \cos x_2 \cos x_3] \sum_n \delta(t-n), \quad (22)$$

let us consider the evolution of a wave function Ψ with the initial condition,

$$\Psi(x_1, x_2, x_3, t=0) \equiv \Xi(x_1, t=0) \delta(x_2 - \varphi_2) \delta(x_3 - \varphi_3). \quad (23)$$

The initial state being perfectly localized in x_2 and x_3 , it is entirely delocalized in the conjugate momenta p_2 and p_3 and can thus be seen as a “plane source” [42] in momentum space.

From a stroboscopic point of view, the time evolution of Ψ is determined by the evolution operator over one period

$$\mathcal{U} = e^{-iK \cos x_1 (1 + \varepsilon \cos x_2 \cos x_3)/\hbar} \times e^{-i(p_1^2/2 + \omega_2 p_2 + \omega_3 p_3)/\hbar}. \quad (24)$$

It is then straightforward to see that the 3D-wave function Ψ at time t is related to its initial condition as

$$\begin{aligned} \Psi(x_1, x_2, x_3, t) &= \mathcal{U}^t \Psi(x_1, x_2, x_3, t=0) \\ &= \Xi(x_1, t) \delta(x_2 - \varphi_2 - \omega_2 t) \delta(x_3 - \varphi_3 - \omega_3 t), \end{aligned} \quad (25)$$

with

$$\Xi(x_1, t) \equiv \prod_{t'=1}^t e^{-iK \cos x_1 [1 + \varepsilon \cos(\varphi_2 + \omega_2 t') \cos(\varphi_3 + \omega_3 t')]/\hbar} \times e^{-ip_1^2/2\hbar} \Xi(x_1, t=0). \quad (26)$$

On the other hand, consider now the evolution of an initial wave function $\psi(x, t=0)$ with the Hamiltonian H_{qp} of the quasiperiodic kicked rotor. It is also determined by an evolution operator from kick to kick, but now this evolution operator $U_{\text{qp}}(t; t-1)$ depends on time since the Hamiltonian H_{qp} [Eq. (20)] is not time periodic

$$U_{\text{qp}}(t; t-1) = e^{-iK \cos x [1 + \varepsilon \cos(\varphi_2 + \omega_2 t) \cos(\varphi_3 + \omega_3 t)]/\hbar} \times e^{-ip^2/2\hbar}. \quad (27)$$

The wave function $\psi(t)$ at time t is obtained by applying successively $U_{\text{qp}}(t'; t'-1)$ for t' from 1 to t

$$\psi(x, t) = \prod_{t'=1}^t U_{\text{qp}}(t'; t'-1) \psi(x, t=0). \quad (28)$$

From Eqs. (25)–(28), it follows that $\psi(x, t)$ and $\Xi(x_1, t)$ follow exactly the same evolution. Consequently, the dynamics of the quasiperiodic kicked rotor is *strictly* equivalent to that of a 3D kicked rotor with a plane source. Our experiment with the quasiperiodic kicked rotor can be seen as a localization experiment in a 3D disordered system, where localization is actually observed in the direction perpendicular to the plane source [21]. In other words, the situation is thus comparable to a transmission experiment where the sample is illuminated by a plane wave and the exponential localization is only measured along the wave-vector direction. Therefore, the behavior of the wave function ψ subjected to the quasiperiodic kicked rotor Hamiltonian H_{qp} [Eq. (20)], depicts *all* the properties of the dynamics of the quantum 3D kicked rotor [Eq. (22)].

The Hamiltonian \mathcal{H} [Eq. (22)] is invariant under the following transformation product of time reversal with parity:

$$T: t \rightarrow -t, \mathbf{x} \rightarrow -\mathbf{x}, \mathbf{p} \rightarrow \mathbf{p}, \quad (29)$$

which is relevant for dynamical localization [43,44]. The evolution of the states according to the Hamiltonian [Eq. (20)] is governed by the operator \mathcal{U} [Eq. (24)], which belongs to the circular orthogonal ensemble class [45,46], with the additional constraint at $t=0$ [Eq. (23)]. Of course, the transformation (29) amounts to changing (φ_2, φ_3) to $(-\varphi_2, -\varphi_3)$ into the constraint (23), i.e., to starting from a different wave function. On the other hand, from Eq. (25), one clearly sees that after t steps, the constraint reads $\delta(x_2 - \tilde{\varphi}_2) \delta(x_3 - \tilde{\varphi}_3)$, with

$$\tilde{\varphi}_2 = \varphi_2 + \omega_2 t \quad \tilde{\varphi}_3 = \varphi_3 + \omega_3 t. \quad (30)$$

Since the frequencies ω_2 and ω_3 are incommensurate, the preceding equation immediately tells us that, along the time evolution, the constraint on the wave function can be arbitrary close to any phases (φ'_2, φ'_3) [47]. This way, the time evolution results in an average over (almost) all possible phases, showing thus that the localization properties are independent of a particular choice (φ_2, φ_3) , but only depend on

the operator \mathcal{U} . Therefore, the dynamical properties of the present quasiperiodic kicked rotor also belong to the orthogonal ensemble.

It should be noted that the 3D aspect comes from the presence of three frequencies in the dynamical system: the usual “momentum frequency” $\hbar k$ present in the standard kicked rotor equation (6) and two additional time frequencies ω_2 and ω_3 . Thus, increasing the number of incommensurate frequencies allows one to tune the effective dimensionality of the system.

Let us now consider the conditions for the observation of Anderson localization with the quasiperiodic kicked rotor. As for the standard kicked rotor, the Floquet states of the time-periodic 3D Hamiltonian \mathcal{H} [Eq. (22)] can be mapped onto a 3D Anderson-like model

$$\epsilon_{\mathbf{m}} \Phi_{\mathbf{m}} + \sum_{\mathbf{r} \neq 0} W_{\mathbf{r}} \Phi_{\mathbf{m}-\mathbf{r}} = -W_0 \Phi_{\mathbf{m}}, \quad (31)$$

where $\mathbf{m} \equiv (m_1, m_2, m_3)$ and \mathbf{r} label sites in a 3D cubic lattice, the on-site energy $\epsilon_{\mathbf{m}}$ is

$$\epsilon_{\mathbf{m}} = \tan \left\{ \frac{1}{2} \left[\omega - \left(k \frac{m_1^2}{2} + \omega_2 m_2 + \omega_3 m_3 \right) \right] \right\}, \quad (32)$$

and the hopping amplitudes $W_{\mathbf{r}}$ are coefficients of a threefold Fourier expansion of

$$W(x_1, x_2, x_3) = \tan[K \cos x_1 (1 + \varepsilon \cos x_2 \cos x_3)/2\hbar]. \quad (33)$$

An obvious necessary condition for the observation of localization effects is that $\epsilon_{\mathbf{m}}$ is not periodic. This is achieved if $(\hbar k, \omega_2, \omega_3, \pi)$ are incommensurate. Of course, the presence of *disorder* in the diagonal energy $\epsilon_{\mathbf{m}}$ is crucial to observe Anderson localization. When $\hbar k$ is incommensurate with 2π , due to the presence of a nonlinear dispersion in the m_1 direction, the classical dynamics can become chaotic with diffusive spreading in *all* \mathbf{m} directions [26,48]. A typical numerical simulation is shown in Fig. 1: the classical motion is almost perfectly diffusive along the three p_i coordinates with a characteristic Gaussian shape in each direction. From Eq. (33), it is clear that hopping along the directions “2” and “3” is diminished by a factor ε compared to hopping along direction “1.” Not surprisingly, diffusion along p_1 is slightly faster than along p_2 and p_3 . The quasiperiodically kicked rotor is thus analogous to an anisotropic Anderson model [49–51].

When those conditions are verified, localization effects as predicted for the 3D Anderson model are expected, namely, either a diffusive or a localized regime. Localized states would be observed if the disorder strength is large as compared to the hopping. In the case of the model (31), the amplitude of the disorder is fixed, but the hopping amplitudes can be controlled by changing the stochasticity parameter K (and/or the modulation amplitude ε): $W_{\mathbf{r}}$ is easily seen to increase with K . In other words, the larger the K , the smaller the disorder. One thus expects to observe diffusive regime for large stochasticity or/and modulation amplitude (small disorder) and localized regime for small K or/and ε (large disorder). It should be emphasized that there is no

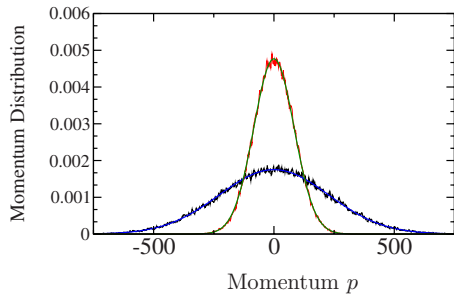


FIG. 1. (Color online) Classical diffusive motion for the 3D kicked rotor (22). The initial state is localized around the origin. After 1000 kicks, the classical momentum distribution (noisy black lower and red upper curves) has the Gaussian shape characteristic of a diffusive motion. The blue lower and green upper curves are fits by a Gaussian, which do not show any statistically significant deviation. The noisy black lower (respectively, red upper) curve is the momentum distribution along p_1 (respectively, p_2). The distribution along p_3 is identical to that along p_2 . The anisotropic diffusion happens because the hopping along the directions “2” and “3” is diminished by a factor ε compared to hopping along direction “1.” Parameters are $K=10$, $\tilde{k}=2.85$, $\varepsilon=0.8$, $\omega_2/2\pi=\sqrt{5}$, and $\omega_3/2\pi=\sqrt{13}$.

stricto sensu mobility edge in our system. Depending on the values of the parameters $K, \tilde{k}, \varepsilon, \omega_2, \omega_3$, all Floquet states are localized or all are delocalized. The boundary of the metal-insulator transition is in the $K, \tilde{k}, \varepsilon, \omega_2, \omega_3$ space. As seen below, K and ε are the primarily important parameters.

In an analytical work on a similar problem [47], Basko *et al.* showed that the weak dynamical localization regime of a d -frequency quantum dot system is similar to the weak localization in a d -dimensional Anderson model. This work confirms the equivalence between our system and the 3D-Anderson model. The above arguments were also validated numerically [26,48].

Numerical simulations of the evolution of the quasiperiodically kicked rotor are straightforward. The free evolution between consecutive pulses is diagonal in momentum representation, while the kick operator is diagonal in position representation (whatever the kick strength, constant, or quasiperiodic). Switching between momentum and position representation is easily done through a fast Fourier transform. We are thus able to compute the evolution of a large number of initial states (typically one thousand) over a very long time (typically up to one million kicks, much more than in the experiment). All numerical results shown below have been carefully checked for convergence. Except when explicitly stated, averaging over the quasimomentum β has been performed, in accordance with the experimental realization.

III. EXPERIMENTAL REALIZATION WITH ATOMIC MATTER WAVES

A. Experimental setup

Our experimental setup has been described in detail in previous publications [52–55] and was used in various investigations on the quasiperiodic kicked rotor [56–59]. Briefly,

our experiments are performed with cold cesium atoms produced in a standard MOT. A long Sisyphus-molasses phase (25 ms) allows us to obtain 10^7 atoms at a measured temperature of $3.2 \mu\text{K}$. The velocity distribution of the atoms is well modeled by an incoherent sum of plane waves forming a Gaussian of full width at half maximum (FWHM) equal to $8\hbar k_L$, which is much narrower than the expected localization length. The MOT beams and magnetic field are turned off and the sequence of kicks is applied to the atoms. The beam forming the standing wave passes through an acousto-optical modulator driven by rf pulse synthesizers, which generates the kicks at a typical frequency of $1/T_1=36 \text{ kHz}$ (which corresponds to $\tilde{k}=2.89$), of duration $\tau=900 \text{ ns}$ and with a raising time of 50 ns. The modulation is thus an almost perfect square, at the time scale of the atomic motion, and its duration and period can be set by a microcomputer. The beam is then injected in an optical fiber that brings it to the interaction region, and the standing wave is obtained simply by back reflection of this beam. The standing wave has a typical power of 160 mW, its profile intensity has a FWHM of 1.5 mm, and it is far off resonant (7.3 GHz to red, or $1.4 \times 10^3 \Gamma$), in order to reduce spontaneous emission. The corresponding stochasticity parameter is $K \approx 15$.

A very interesting property of our system (as compared to solid-state systems) is that the wave function is accessible (or at least its square modulus). We measure the atomic velocity distribution by velocity-selective Raman stimulated transitions, which are sensitive to the atomic velocity via Doppler effect, allowing an optimal velocity resolution of about 2 mm/s. A Raman pulse detuned of δ_R with respect to the Raman resonance transfers the atoms in the velocity class $v = \delta_R/(2k_R) - v_R$ with $v_R = \hbar k_R/M$ (k_R is the wave number of the Raman beams) from the $F_g=4$ to the $F_g=3$ ground-state hyperfine sublevel. A beam resonant with the $F_g=4 \rightarrow F_e=5$ transition is then applied to push the remaining atoms out of the interaction region. The $F_g=3$ atoms are then optically pumped to the $F_g=4$ sublevel and interact with a resonant probe beam. The absorption signal is thus proportional to the population of the $F_g=4$ level, thus, to the population of the selected velocity class. The whole sequence then starts again with a different value of the Raman detuning to probe a new velocity class, allowing a reconstruction of the velocity distribution [53,55].

B. Decoherence sources

Any quantum experiment must consider decoherence sources that destroy quantum interference effects (in our case, localization) re-establishing a diffusive dynamics. The most important sources of decoherence in our experiment are (i) atomic collisions, (ii) spontaneous emission, and (iii) the deviation of the standing wave from strict horizontality.

For an isolated system described by a single wave function, phase coherence between different positions is “perfect.” When the system is weakly coupled to an external bath, it cannot be any longer described by a single wave function; the most convenient description usually involves a density matrix ρ . Nondiagonal matrix elements of the type $\langle x|\rho|x' \rangle$ quantify the degree of coherence of the system be-

tween positions x and x' . As a general rule, the effect of the external bath is to make the nondiagonal elements of the density matrix to decay relatively rapidly, more rapidly than the diagonal elements: this is decoherence (not to be confused with dissipation) [60]. Effects like Anderson localization are due to subtle destructive interference among various components of the wave function, which inhibit the classically allowed transport: they are thus very sensitive to decoherence. One usually quantify the strength of decoherence effects by defining a phase-coherence time, the characteristic time over which the nondiagonal elements of the density matrix decay because of coupling to the external bath. In our case, the nondiagonal element of interest is between eigenstates $|p\rangle$ and $|p'\rangle$ located at a typical distance $|p-p'|$ comparable to the localization length in momentum space.

Localization effects can be observed only for times shorter than the phase-coherence time [61]. Beyond the phase-coherence time, interference effects are killed and classical-like diffusive dynamics sets in. In the following, we shall express the characteristic times of the decoherence processes (i), (ii), and (iii), as functions of the experimental parameters to show that they can be set large enough for localization effects to be observable.

In atom-atom collisions, the dominant effect is that of collisions between cold atoms, the density of the cloud being around 8 orders of magnitude larger than the density of the background hot gas. A cloud density of 10^{12} cm $^{-3}$ with a mean velocity of 1 cm/s and a collision cross section of 6×10^{-11} cm 2 gives a collision rate of ≈ 60 s $^{-1}$, or 1.6×10^{-3} per kick; the collision phase-coherence time is thus ~ 600 kicks.

In order to have a better idea of the decoherence effect induced by spontaneous emission, let us consider the temporal evolution of an initial plane-wave function: $\psi(p, t=0) = \delta(p-p_0)$ evolving with the KR Hamiltonian (6). After dynamical localization sets in, the momentum distribution ceases to expand because of destructive interference between the various components of the wave function. Spontaneous emission brings a random recoil to the atomic momentum which is not an integer multiple of $2\hbar k_L$. Thus, the quasimomentum β performs a random jump. As the phase factors involved in the free evolution depend on the quasimomentum, the relative phases between interfering paths are scrambled, resulting in a new transient diffusive behavior for another duration of τ_{loc} . DL is thus expected to be destroyed if spontaneous emission is regularly repeated. Note that a single spontaneous emission event completely breaks the phase coherence, implying that the phase-coherence time is simply the inverse of the spontaneous emission rate.

Spontaneous emission tends to re-establish a diffusive evolution with a diffusion constant that is roughly $\eta\hbar^2$, where $\eta = \Gamma\Omega^2\tau/8\Delta_L^2$, is the spontaneous emission rate expressed in photons per kick, which can be cast in the more useful form $\eta = (\Gamma\tau/8)(I/I_s)(\Gamma/\Delta_L)^2$, where I is the intensity and $I_s \approx 2.2$ mW/cm 2 is the transition saturation intensity. Around the transition ($K \approx 6$), the experimental values indicated above give $\eta \approx 2.1 \times 10^{-3}$ s $^{-1}$ or a typical phase-coherence time of ~ 500 kicks.

Another effect leading to the destruction of localization is the standing-wave deviation from horizontality. In this case,

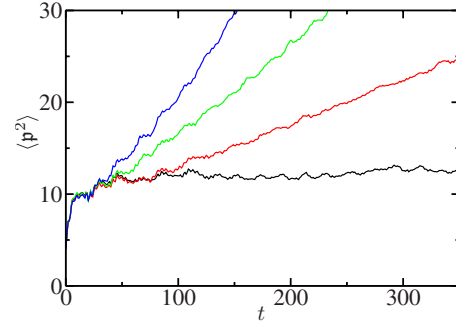


FIG. 2. (Color online) Gravity effects on a slightly inclined kicked rotor (34). The deviation of the standing wave from horizontality is $\alpha=0^\circ$ (black lower curve), $\alpha=0.1^\circ$ (red lower middle curve), $\alpha=0.4^\circ$ (green upper middle curve), and $\alpha=1^\circ$ (blue upper curve). The stochasticity parameter is taken as $K=5$ and the effective Planck constant is $\hbar=2.85$. The dynamics of an initial thermal state is simulated and the corresponding mean kinetic energy is plotted versus time. For angles larger than 0.1° , the slow drift of momentum induces a diffusive behavior clearly visible on the time scale of the experiment.

a gravity term must be added in the Hamiltonian (6)

$$H_g = \frac{p^2}{2} - \eta_g x + K \cos x \sum_n \delta(t-n). \quad (34)$$

The dimensionless gravity term η_g is

$$\eta_g = \frac{mgT_1}{2\hbar k_L} \sin \alpha, \quad (35)$$

with g as the gravity acceleration and α as the angle between the horizontal direction and the standing wave. The physical interpretation is quite clear: $mgT_1 \sin \alpha$ is the additional momentum transferred to the atoms between two consecutive kicks, which must be compared to the width of the Brillouin zone $2\hbar k_L$.

The gravity term $-\eta_g x$ breaks the spatial periodicity of the Hamiltonian and, consequently, the conservation of the quasimomentum $\beta\hbar k$. It actually produces a drift of the quasimomentum at constant rate $-\eta_g$, whose effect is to break dynamical localization. Indeed, the destructive interference between various components of the momentum wave function—responsible for dynamical localization—is partially destroyed by the quasimomentum drift, as the various phase factors accumulated during the free evolution between two consecutive kicks, $\exp[-i(m+\beta\hbar k)^2/2\hbar k]$ also drift. The net result is a residual diffusion constant, depending on η_g . Although this is not strictly a decoherence effect (the whole evolution is fully phase coherent), it similarly destroys dynamical localization. We thus define the phase-coherence time τ_g as the time needed to double $\langle p^2 \rangle$ compared to the dynamically localized situation. Numerical simulations taking into account the gravity effect confirm the discussion above (see Fig. 2). If the standing wave deviates from horizontality by an angle $\alpha=1^\circ$, then $\tau_g \approx 120$ kicks whereas when the angle $\alpha=0.1^\circ$, $\tau_g \approx 350$ kicks. In the time scale of the experiment (150 kicks), the deviation from horizontality must be less than 0.1° . This decoherence effect is rather im-

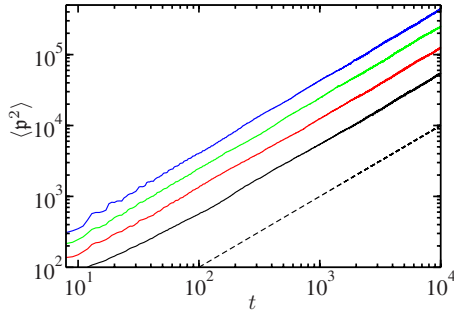


FIG. 3. (Color online) Classical chaotic diffusion for the quasi-periodic kicked rotor (22). The dynamics of an initial thermal distribution of classical particles is simulated and the corresponding mean kinetic energy is plotted versus time (number of kicks). The stochasticity parameter K (the modulation amplitude ϵ) varies linearly between 4 and 9 (0.1 and 0.8), following the experimental path (Fig. 6). The dashed line of slope 1 demonstrates the linear increase of $\langle p^2 \rangle$ vs time t . No classical localization effects are observed. The chaotic diffusion is characteristic of the presence of pseudodisorder in the quasiperiodic kicked rotor, leading to a pseudorandom walk in momentum space.

portant. To the best of our knowledge, its importance was not fully appreciated in previous experiments. A detailed discussion of this effect will be presented elsewhere [62].

C. Conditions for the observation of localization effects

We now discuss the conditions that must be satisfied in order to observe localization effects experimentally.

First, the system must present some kind of disorder. As discussed in Sec. II C, this means that \hbar , ω_2 , and ω_3 and π must be incommensurate. This is achieved if we take $\hbar = 2.89$, $\omega_2 = 2\pi\sqrt{5}$, and $\omega_3 = 2\pi\sqrt{13}$. A more detailed discussion concerning the choice of these parameters will be given in Sec. VI B.

Second, in order to observe dynamical localization effects instead of trivial classical localization, we must be in a regime where the classical system has no KAM barriers, which can prevent the classical diffusive transport. For the standard periodic KR, full chaos is obtained for $K \geq 4$. In order to determine the corresponding threshold for the quasiperiodic system, we performed numerical simulations of the classical dynamics corresponding to Eq. (22), for various values of the stochasticity parameter. The dynamics is found to be fully diffusive for $K \geq 2$, a considerably smaller value than for the standard KR. In particular, no classical localization effects due to KAM barriers are observed for $K \geq 2$. In any case, the experiments and the numerical simulations in the following are all performed for $K > 4$, where the classical dynamics is diffusive (see Fig. 3).

Third, short enough pulses must be used that they can be considered as delta pulses [63]. Numerical simulations of the quasiperiodic kicked rotor with a finite pulse duration $\tau = 0.9 \mu\text{s}$ and a thermal initial momentum distribution show that less than 1% of the atoms are sensitive to the duration of the pulses. Only atoms in the tails of the momentum distribution have sufficiently large atomic velocity to move by a

significant fraction of λ_L during the pulse, thus, feeling a smaller effective kick.

Fourth, a sufficiently narrow initial state must be prepared in order to observe dynamical localization, i.e., the freezing of the initial diffusive expansion of the wave function into an exponentially localized state. A sufficient condition is that the initial width of the momentum distribution be smaller than the localization length. In our system, we have an initial momentum distribution of half-width $2\hbar k$. This is comparable to the shortest localization length at the lowest $K=4$ value, as experimentally proved (see inset of Fig. 5). A consequence is that, in this regime, the exponential shape of the wave function after dynamical localization is established is slightly rounded at the tip. For higher values—say $K > 5$ —the initial width of the atomic wave function can be safely neglected.

Finally, decoherence processes must be kept small during the experiment. The large detuning of the standing wave allows to keep the spontaneous emission rate very small, i.e., the corresponding phase coherence is large as compared to the duration of the experiment. A good control on the horizontality of the standing wave ensures that gravity do not lead to a destruction of localization effects on the time scale of the experiment.

IV. EXPERIMENTAL OBSERVATION OF THE DISORDER-INDUCED METAL-INSULATOR TRANSITION

In a typical experimental run, we apply a sequence of kicks to the atomic cloud and measure its dynamics. In the localized regime, the evolution of its momentum distribution is “frozen” after the localization time (typically on the order of 12 kicks at low K) into an exponential curve $\exp(-|p|/\ell)$. In the diffusive regime, the initial Gaussian shape is preserved and the distribution gets broader as kicks are applied, corresponding to a linear increase in the average kinetic energy. Figure 4 shows the experimentally observed momentum distributions, an exponentially localized distribution for small K and ϵ (blue peaked curve), characteristic of dynamical localization, and a broad Gaussian-shaped distribution for large K and ϵ (red broad curve), characteristic of the diffusive regime.

Measuring the whole momentum distribution takes too much time: one must repeat the whole sequence (from the preparation of a new atom cloud up to the Raman measurement of the velocity distribution) for each velocity class. Moreover, for each time step, a complete momentum distribution must be measured. Fortunately, it is sufficient and much easier to measure the population $\Pi_0(t)$ of the zero velocity class, as $\Pi_0^{-2}(t)$ is proportional to $\langle p^2 \rangle(t)$ (the total number of atoms is constant). The proportionality factor between $\Pi_0^{-2}(t)$ and $\langle p^2 \rangle(t)$ depends on the detailed shape of the momentum distribution and is thus different in the localized and diffusive regime, but this small difference is a small correction to the main phenomenon: divergence of the localization length near the transition.

Note that, strictly speaking, the proportionality between $\Pi_0^{-2}(t)$ and $\langle p^2 \rangle(t)$ breaks at criticality due to the multifractal character of critical states [64]. However, on the time scale of the experiment ($t=150$ kicks), the deviation from strict

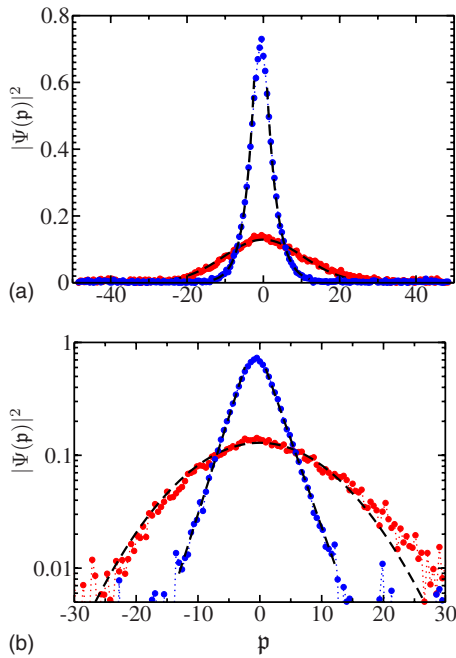


FIG. 4. (Color online) Experimentally measured momentum distributions after 150 kicks, exponentially localized in the insulator region (blue peaked) and Gaussian in the diffusive (metallic) region (red broad). (a) Linear scale; (b) log scale. For both curves $\hbar = 2.89$, for the localized distribution (blue peaked) $K=5.0$ and $\epsilon = 0.24$, for the Gaussian distribution (red broad) $K=9.0$ and $\epsilon=0.8$.

proportionality is seen (numerically) to be negligible. At longer times (thousands or millions of kicks), the effect of multifractality is visible and quantitatively measurable. This is beyond the scope of this paper and will be analyzed elsewhere [65].

For each run, a value of $\Pi_0(t)$ is recorded after a given number of kicks is applied, then the measurement sequence starts again with the next number of kicks. We also record the background signal obtained by not applying the Raman detection sequence and the total number of atoms in the cold-atom cloud. These signals are used to correct the experimental data from background signals and long-term drifts of the cloud population.

Figure 5 shows the experimentally measured $\Pi_0^{-2}(t)$ in the localized and diffusive regimes. It clearly shows the initial diffusive phase and the freezing of the quantum dynamics in the localized regime (blue lower curve in Fig. 5). Along with the observation of an exponential localization of the wave function in Fig. 4, this constitutes a clear-cut proof of the observation of dynamical localization. In the diffusive regime, $\Pi_0^{-2}(t)$ is seen to increase linearly with time (red upper curve in Fig. 5), corresponding to the Gaussian red broad curve in Fig. 4.

After having observed Anderson localization for strong effective disorder strength and diffusive transport for small effective disorder, the next step is to walk the way between these two regimes and explore the phase transition expected (numerically) to take place along a critical line in the plane $(K, \epsilon > 0)$ (Fig. 6). In order to confine the transition to a narrow range of parameters, we choose a path that crosses the critical curve (Fig. 6) “at a right angle;” we thus vary

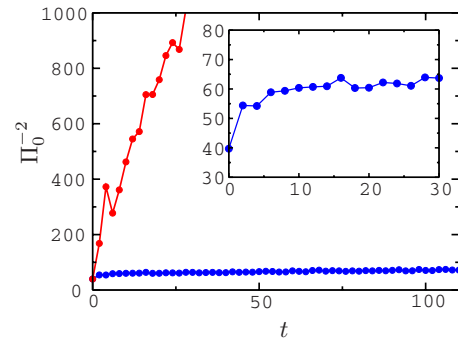


FIG. 5. (Color online) Temporal dynamics of the quasiperiodic kicked rotor. We experimentally measure the population $\Pi_0(t)$ of the zero-momentum class as a function of time (number of kicks) and plot the quantity $\Pi_0^{-2}(t) \propto \langle p^2 \rangle(t)$. Clearly, it tends to a constant in the localized regime (blue lower curve corresponding to $K=4$ and $\epsilon=0.1$) and increases linearly with time in the diffusive regime (red upper curve corresponding to $K=9$ and $\epsilon=0.8$). The inset shows the behavior close to the localization time. $\hbar = 2.89$.

simultaneously K and ϵ along a line going from $K=4$, $\epsilon = 0.1$ in the localized region to $K=9$, $\epsilon=0.8$ in the diffusive region; the critical line is then crossed at $K=K_c=6.6$.

A simple way to investigate the phase transition is the following [26]. In the localized regime, wait for a time longer than the localization time so that a localized frozen wave function is observed, then measure its localization length. One can in such a way study the behavior of the localization length vs disorder: at criticality, it should diverge as $\ell \sim (K-K_c)^{-\nu}$. This would give the critical stochasticity parameter ν and the critical exponent ν . However, we cannot proceed that way in our case because when one approaches the critical point from the insulator side, the localization time diverges as $\tau_\ell \sim \ell^3 \sim (K-K_c)^{-3\nu}$ in three dimensions (see below). In our system, a localized momentum distribution would be observable in the vicinity of the transition only for prohibitively large numbers of kicks, which are, in practice, limited to 150, essentially because of

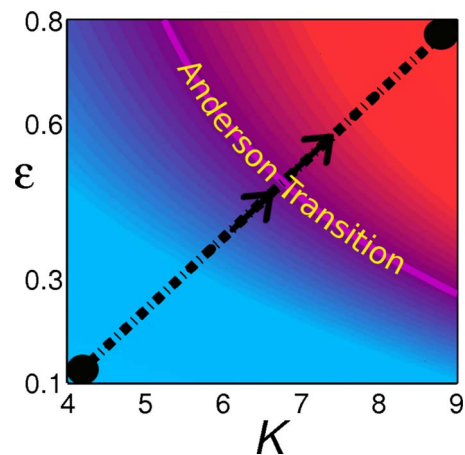


FIG. 6. (Color online) Phase diagram of the quasiperiodic kicked rotor, from numerical simulations. The localized (insulator) region is shown in blue (left bottom corner); the diffusive (metallic) region is shown in red (right top corner). The experimental parameters are swept along the diagonal dash-dotted line.

decoherence effects and because the free fall of the atom cloud takes it out of the standing wave. Consequently, it is vain to investigate experimentally the Anderson transition only from *static* properties, such as the divergence of the localization length at criticality, which could be obtained only for $t \gg \tau_{\text{loc}}$. Fortunately, there is another way to observe the Anderson transition, which we shall present in the following sections.

V. CHARACTERIZATION OF THE ANDERSON PHASE TRANSITION

Finite-time effects act as finite-size effects do on finite-size samples subjected to phase transitions. Numerical simulations of the Anderson transition on the standard 3D-Anderson model are necessarily performed on finite-size samples of finite size L . In the vicinity of the transition, the localization length ℓ [see Eq. (2)] diverges and thus can greatly exceed L . In this regime, L acts as an upper bound for the effectively observed localization length ℓ_L . This smooths the transition, no divergence of the localization length can be *directly* observed on a finite-size sample. In order to overcome this limitation, a powerful real-space renormalization method called finite-size scaling [9,10] was introduced. This method is based on a single parameter scaling hypothesis [8] and allows to extrapolate from the scaling behavior of ℓ_L versus L the asymptotic value of the localization length ℓ corresponding to $L \rightarrow \infty$. We can generalize static scaling laws to cover our time-dependent problem (see [66] for a similar approach in percolation theory). The single parameter scaling theory [8], successfully used for the standard 3D Anderson model [9,10], can be applied to analyze our experimental and numerical data and, especially, to determine the critical properties of the Anderson transition that we observe, i.e., the critical exponents.

A. Scaling law at finite time

Knowing the asymptotic behavior when $t \rightarrow \infty$ is not enough, an additional time-dependent property is needed too, which we shall investigate now. For K far above K_c one observes normal diffusion $\langle p^2 \rangle \propto t$, whereas for K far below K_c , the quantum dynamics freezes, at sufficiently long times. Following the standard analysis of the Anderson transition, we make the hypothesis that the transition that we observe for the quasiperiodically kicked rotor follows a one-parameter scaling law [67] (the validity of this scaling hypothesis will of course be checked at the end of the analysis). At the critical point, a third kind of dynamics, namely, anomalous diffusion, with $\langle p^2 \rangle \sim t^k$ $k \neq 1$, is expected. Let us consider in greater detail the behavior very close to K_c , where these three different laws merge.

In the localized regime, for sufficiently long times, the behavior depends only on the localization length which diverges as K goes to K_c

$$\langle p^2 \rangle \sim \ell^2 \sim (K_c - K)^{-2\nu} \text{ (for } K < K_c), \quad (36)$$

where ν is the localization length critical exponent.

For $K > K_c$, the mean kinetic energy increases linearly with time and the proportionality constant is the diffusion coefficient $D(K)$. For $K < K_c$, $\langle p^2 \rangle$ is bounded by Eq. (36) and there is no diffusion. Thus, $D(K)$ vanishes below K_c . A different critical exponent s is used to describe how $D(K)$ goes to zero above threshold

$$D(K) \sim (K - K_c)^s \quad \text{(for } K > K_c). \quad (37)$$

We shall now find a single expression presenting these two limit behaviors and also displaying anomalous diffusion at the critical point. We note that according to the theory of phase transitions in finite-size samples, a scaling can be applied to $\langle p^2 \rangle$ depending on the two variables $1/t$ and $(K - K_c)$, both going to zero. We thus use the general scaling law

$$\langle p^2 \rangle = t^{k_1} F[(K - K_c)t^{k_2}], \quad (38)$$

with $F(x)$ as an unknown scaling function. The exponents k_1 and k_2 can be determined as follows.

In the diffusive regime, for long enough times, we must recover the diffusion law with $D \sim (K - K_c)^s$ [Eq. (37)]; hence, for $x \gg 1$, the scaling function $F(x)$ should scale as x^s

$$\langle p^2 \rangle \sim t^{k_1 + s k_2} (K - K_c)^s. \quad (39)$$

As in the diffusive regime $\langle p^2 \rangle \sim t$, we must have $k_1 + s k_2 = 1$.

In the localized regime, on the other hand, one must recover $\langle p^2 \rangle \sim (K_c - K)^{-2\nu}$ [Eq. (36)] for sufficiently long times. Thus, for $x \rightarrow -\infty$, $F(x) \rightarrow (-x)^{-2\nu}$, giving

$$\langle p^2 \rangle = t^{k_1 - 2\nu k_2} (K_c - K)^{-2\nu}, \quad (40)$$

which is compatible with Eq. (36) only if $k_1 = 2\nu k_2$. These two relations determine k_1 and k_2 in terms of the physically more meaningful critical exponents s and ν ,

$$k_1 = \frac{2\nu}{s + 2\nu},$$

$$k_2 = \frac{1}{s + 2\nu}.$$

In the standard Anderson model, the critical exponents are related by Wegner's scaling law [6]

$$s = (d - 2)\nu, \quad (41)$$

with d being the dimensionality of the system. For our system, one obtains

$$k_1 = 2/3; \quad k_2 = 1/3\nu. \quad (42)$$

We therefore expect at the critical-point anomalous diffusion with $\langle p^2 \rangle = t^{k_1} F(0) \sim t^{2/3}$. We present in the next subsection a numerical and experimental validation of this prediction.

B. Critical anomalous diffusion

We verified numerically that the critical behavior, corresponding to the anomalous diffusion in $t^{2/3}$ is observed up to a very large number of kicks ($t = 10^6$). The purple middle curve of Fig. 7 displays the time evolution of $\langle p^2 \rangle$ from nu-

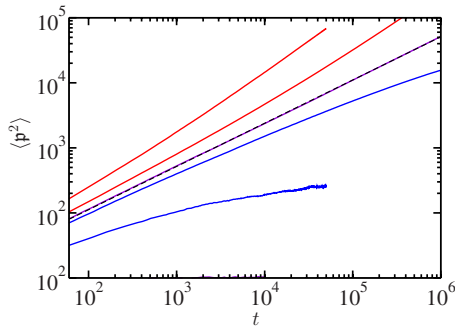


FIG. 7. (Color online) Numerically simulated time evolution of $\langle p^2 \rangle$ for the quasiperiodic kicked rotor. At the critical point $K=K_c \approx 6.4$ (purple middle curve), anomalous diffusion $\langle p^2 \rangle \sim t^{2/3}$ is clearly observed, as expected from theoretical arguments (cf. text). The log-log plot of the critical curve is very well fitted by a straight line of slope 0.664 (black dashed line). In the vicinity of the transition, the dynamics departs from the anomalous diffusion to tend gradually either to a diffusive dynamics (red upper curves corresponding to $K > K_c$ bending upward for large t) or to a localized dynamics (blue lower curves corresponding to $K < K_c$ bending downwards for large t). Other parameters are $\hbar=2.85$, $\omega_2=2\pi\sqrt{5}$, and $\omega_3=2\pi\sqrt{13}$.

merical simulations for the stochasticity parameter $K=6.4$. Anomalous diffusion $\langle p^2 \rangle \sim t^{2/3}$ is clearly seen from the log-log plot over 4 orders of magnitude, which is very well fitted by a straight line of slope 0.664. Other curves, for different K , tend at long times to bend either horizontally (below K_c) or toward slope unity (above K_c). This is a clear proof that we face here a true phase transition and not a smooth crossover. Note also that the fact that the numerically measured critical slope is very close to the theoretical prediction $2/3$ implies that the Wegner's scaling law $s=\nu$ is valid at an accuracy better than 1%.

Figure 8 displays the experimental evolution of $\Pi_0^{-2}(t) \sim \langle p^2 \rangle$ versus time. The critical curve (middle curve corresponding to $K \approx 6.4$) in purple is well fitted by the relation $\Pi_0^{-2}(t) = A + Bt^{2/3}$ [see Fig. 8(a)]. Figure 8(b) displays in log-log scale the experimental data $\Pi_0^{-2}(t)$ vs t . The algebraic dependence (with exponent $2/3$) of the critical dynamics is again clearly visible. In all plots in Figs. 8, the red upper curves evidence the above-criticality diffusive behavior and the blue lower curves the below-criticality localized behavior.

From renormalization theory, we know that the critical behavior shows the existence of a fixed hyperbolic point [16]. It is a fixed point because the critical behavior remains the same at all times (opposite to the localized case, for example, for which a characteristic time can be defined, the localization time), and it is a hyperbolic point since the localized dynamics close to criticality will follow only for a finite time the anomalous diffusion with exponent $2/3$ and will progressively tend to a localized behavior for large enough time. The rate at which the behavior changes is related to the critical exponent of the phase transition ν .

An efficient way to observe the departing of the dynamics from the critical anomalous diffusion is to consider the quantity

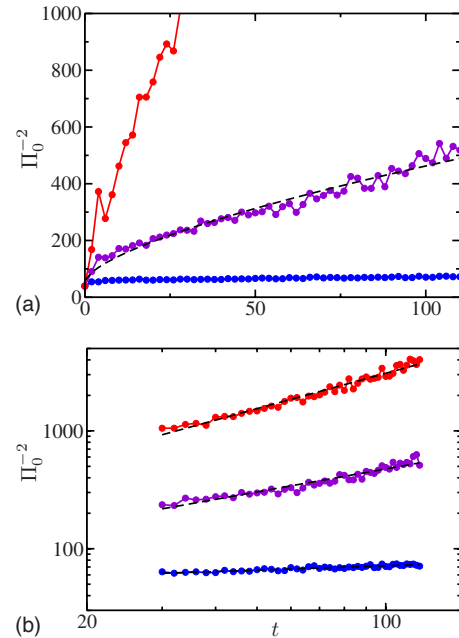


FIG. 8. (Color online) Experimentally observed time evolution of $\Pi_0^{-2} \sim \langle p^2 \rangle$ for the quasiperiodic kicked rotor. Close to the critical point $K=K_c \approx 6.4$ (purple middle curve), anomalous diffusion $\Pi_0^{-2}(t) \sim t^{2/3}$ is clearly observed. (a) The critical anomalous curve is well fitted by $\Pi_0^{-2}(t) = A + Bt^{2/3}$ (black dashed line). The red upper curve evidences the far-above-criticality diffusive behavior ($K=9.0$) and the blue lower curve evidences the far-below-criticality ($K=4.0$) localized behavior. (b) These experimental results show a clear algebraic behavior, with exponent ≈ 0 (blue lower curve, localized regime), $2/3$ (purple middle curve, critical regime), and 1 (red upper curve, diffusive regime), slightly perturbed by decoherence processes responsible for the residual increase in the localized regime. Other parameters are the same as in Fig. 7.

$$\Lambda = \frac{\langle p^2 \rangle}{t^{2/3}}, \quad (43)$$

or, equivalently, in the case of the experimental data,

$$\Lambda_0 = \frac{1}{\Pi_0^{-2}(t)t^{2/3}}, \quad (44)$$

as a function of time. This is illustrated in Fig. 9, which displays $\ln \Lambda$ vs t . The critical behavior can be easily pinpointed. The corresponding (purple middle) curve has a zero slope, as the quantity Λ is (asymptotically) constant at criticality. In the diffusive regime, the quantity Λ increases with time (red upper curves), whereas it decreases in the localized regime (blue lower curves). In the far localized regime, we observe an algebraic dependence $\Lambda(t) \sim t^{-2/3}$ as $\langle p^2 \rangle(t) = 2\ell^2$ for $t > \tau_{loc}$. In the far diffusive regime, the algebraic dependence is $\Lambda(t) \sim t^{1/3}$ as $\langle p^2 \rangle(t) \sim t$.

The above numerical and experimental observations validate the theoretical prediction for the critical behavior: $\langle p^2 \rangle \sim t^{2/3}$. Such critical behavior for the quasiperiodic kicked rotor was predicted using another scaling approach and numerically verified in [48]. It was also numerically observed

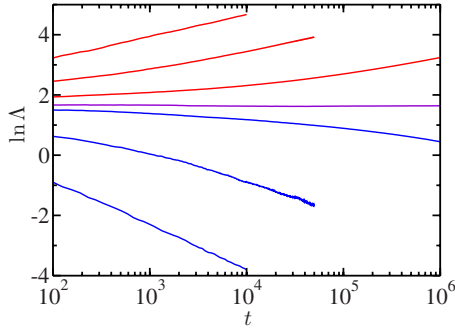


FIG. 9. (Color online) Numerical simulation showing the evolution of the dynamics from the critical behavior toward either a diffusive dynamics or a localized state. Plotting the quantity $\ln \Lambda = \ln(\langle p^2 \rangle t^{-2/3})$ vs $\ln t$ allows to easily distinguish the critical behavior from diffusive or localized behavior: the critical curve (corresponding to $K=K_C \approx 6.4$) has a zero slope; whereas the far localized ($K=4.0$) one has a slope $-2/3$ and the far diffusive ($K=9.0$) one has a slope $1/3$. Other parameters are the same as in Fig. 7.

for a spatially 3D kicked rotor [40] and in the standard 3D Anderson model [67] and put on firm theoretical grounds in [68].

C. Finite-time scaling

We shall now explain the procedure used to verify the scaling of our numerical and experimental data according to the law deduced above

$$\langle p^2 \rangle = t^{2/3} F[(K - K_c)t^{1/3\nu}]. \tag{45}$$

Our method is similar to the finite-size scaling procedure used by MacKinnon and Kramer [9,69] and Pichard and Sarma [10] to numerically study the Anderson transition on finite samples of the 3D Anderson model, but we apply it here to the temporal behavior of the data, thus, the name “finite-time scaling.”

We assume the quantity $\Lambda(K, t) = \langle p^2 \rangle t^{-2/3}$ to be an arbitrary function

$$\Lambda(K, t) = f(\xi(K)t^{-1/3}), \tag{46}$$

where the scaling parameter $\xi(K)$ depends *only* on K , which is the parameter appearing in the one-parameter scaling hypothesis. This scaling assumption is less restrictive than Eq. (45) since no assumption on the dependence of ξ on K is made. We must thus show that the resulting scaling parameter $\xi(K)$ is compatible with Eq. (45).

In the left part of Fig. 10, we display plots of $\ln \Lambda(K, t)$ vs $\ln t^{-1/3}$ for different values of K . For most values of $\ln \Lambda$, several values of $\ln t^{-1/3}$ correspond to the same K value. The only way to conform with the condition (46) is to shift each curve horizontally by a different quantity $\ln \xi(K)$ such that curves corresponding to different values of K overlap. This can be achieved by minimizing the variance of the values $\ln \xi(K)t^{-1/3}$ corresponding to each value of $\ln \Lambda$. The function $\xi(K)$ can be determined by applying a least-square fit to the data.

This minimization procedure does not allow one to compute the absolute scale of $\xi(K)$, as the shifting procedure (see

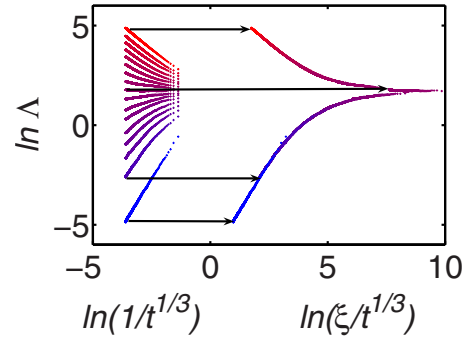


FIG. 10. (Color online) Raw numerical data displayed in the form $\ln \Lambda = \ln(\langle p^2 \rangle t^{-2/3})$ vs $\ln t^{-1/3}$ (on the left). Each curve corresponds to a different stochasticity parameter K . The finite-time scaling procedure consists in shifting horizontally each curve by a quantity $\ln \xi(K)$ so that the curves overlap. This allows one to determine both the scaling function f (on the right) and the scaling parameter $\xi(K)$.

Fig. 10) is invariant under a global shift of the origin. We can thus set the scaling parameter $\xi(K)$ to be equal to the localization length in the strongly localized regime, where the duration of the experiment is much larger than the localization time, and $\langle p^2 \rangle$ converges to its asymptotic value $2\ell^2$. Thus,

$$\Lambda(K, t) = f(\xi(K)t^{-1/3}) = 2\ell^2 t^{-2/3},$$

which implies, if we identify the scaling parameter with the localization length, $\xi(K) \sim \ell$,

$$f(x) = 2x^2.$$

Figures 11(a) and 12(a) show the results of the fitting procedure applied to the numerical data and to the experimental data, respectively. In both cases, the procedure groups all points in a *single* curve, within the accuracy of the data.

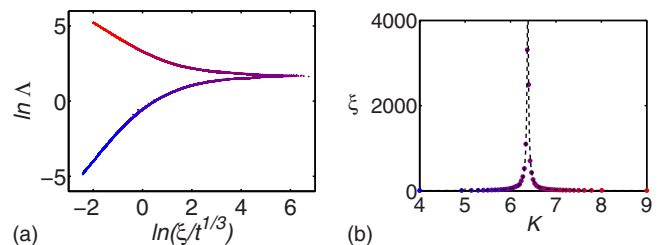


FIG. 11. (Color online) Finite-time scaling applied to the results of numerical simulations of the quasiperiodic kicked rotor. The time evolution of $\langle p^2 \rangle$ is computed as a function of time, from 30 to 10^4 kicks, for several values of K between $K=4$ and $K=9$. The finite-time scaling procedure allows us to determine both the scaling function f (a), clearly displaying an upper branch (red) associated with the diffusive regime, and a lower branch (blue) associated with the localized regime. The dependence of the scaling parameter ξ on K (b) displays a divergent behavior around the critical point $K_c=6.4$, which is the signature of the Anderson phase transition. The dashed line is a fit using Eq. (48). The resulting critical exponent is $\nu = 1.6 \pm 0.1$. Other parameters are $\hbar=2.85$, $\omega_2=2\pi\sqrt{5}$, and $\omega_3=2\pi\sqrt{13}$.

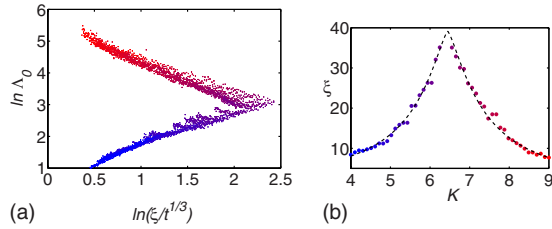


FIG. 12. (Color online) Finite-time scaling applied to the experimental results (from 30 to 150 kicks). The scaling procedure is the same as in Fig. 11. (a) The fact that all experimental points lie on a single curve, with a diffusive (red upper) and a localized (blue lower) branch, is a proof of the relevance of the one-parameter scaling hypothesis. (b) The maximum displayed by the scaling parameter ξ in the vicinity of $K_c=6.4$ is a clear-cut proof of the Anderson transition. Phase-breaking mechanisms (cf. text) smooth the divergence at the critical point. When these effects are properly taken into account, one obtains a critical exponent $\nu=1.4 \pm 0.3$, [the dashed line is a fit with Eq. (48)] compatible with the numerical results. This plot corresponds to 48 experimental runs. Other parameters are as in Fig. 11.

The resulting curve clearly displays two branches, a diffusive (red) and a localized (blue) one, with the critical point being at the tip joining the two branches; this is a signature of the Anderson transition. It also justifies *a posteriori* the scaling hypothesis (46) used for analyzing the data.

The scaling parameter $\xi(K)$ is plotted in Figs. 11(b) and 12(b), for numerical and experimental data, respectively. As stated above, this parameter can be identified to the localization length in the localized regime. In the diffusive regime, it scales as the inverse of the diffusive constant. Indeed, in the far diffusive regime one has $\langle p^2 \rangle = D(K)t$, which implies

$$\Lambda(K, t) = D(K)t^{1/3},$$

$$f(x) = x^{-1},$$

so that $\xi(K) = 1/D(K)$ in the far diffusive regime.

One notes that $\xi(K)$ increases rapidly in the vicinity of the critical value K_c , on both sides of the transition. This corresponds to a divergence of the localization length and to a vanishing of the diffusion constant at criticality (in practice, smoothed by decoherence, see below). This constitutes a clear *experimental* evidence of the Anderson phase transition.

D. Experimental determination of the critical exponent

The behavior of $\xi(K)$ gives a fundamental information about the transition, namely, the value of the localization length critical exponent ν . There is a discrepancy in the literature between the theoretical predictions $\nu=1$ [13], $\nu=1.5$ [70], and the result of numerical simulations $\nu=1.57 \pm 0.02$ [12], which stresses even more the importance of an experimental determination. In this section, we present an unambiguous experimental determination of the critical exponent of the Anderson transition in three dimensions.

The finite-time scaling procedure allows us to extract from finite-time experimental data the localization length ℓ

(corresponding to $t \rightarrow \infty$), which is the order parameter of the Anderson transition. It is given by the scaling parameter $\xi(K)$ and predicted to diverge at criticality with the power law

$$\ell \sim |K - K_c|^{-\nu}. \quad (47)$$

We thus expect that the singularity in $\xi(K)$ can be described by Eq. (47) and to be able to extract the value of the critical exponent ν . This is of primary importance, as there is presently no unambiguous accurate experimental determination of ν for noninteracting particles, and there is a discrepancy in the literature between the theoretical predictions $\nu=1$ [13], $\nu=1.5$ [70], and the result of numerical simulations $\nu=1.57 \pm 0.02$ [12].

When the slope of $\ln \Lambda$ vs $\ln t^{-1/3}$ is small, as it is near the critical point, the scaling procedure tends to round off the singularity in $\xi(K)$. Moreover, decoherence in the experiment produces a cutoff the algebraic divergence. If the system has a finite phase-coherence time τ_ϕ , a new characteristic length [71] $p_\phi = [D\tau_\phi]^{1/2}$ appears in the problem, which sets an upper bound for the observable localization length ℓ and thus smooths its divergence at criticality. In practice, we model such smoothing by introducing a small cutoff on the divergence of $\xi(K)$, which takes into account both the finite-time scaling procedure itself and decoherence effects

$$\frac{1}{\xi(K)} = \alpha |K - K_c|^\nu + \beta. \quad (48)$$

The experimental data have been fitted with this formula (48) [dashed curve in Fig. 12(b)], which gives $K_c \approx 6.4 \pm 0.2$, and a critical exponent $\nu=1.4 \pm 0.3$. In order to compare these results to the ideal case of the perfectly coherent quasiperiodic kicked rotor [Eq. (20)], we also fitted the curve in Fig. 11(b) with Eq. (48); in this case, the cutoff β accounts for limitations of the finite-time scaling procedure. The model (48) fits very well to the numerical data [dashed curve in Fig. 11(b)] and gives the critical stochasticity $K_c \approx 6.4 \pm 0.1$ and the critical exponent $\nu=1.6 \pm 0.2$. The good agreement between the numerical simulations and the experimental results proves that spurious effects (such as decoherence) are well under control. Moreover, the experimental value we obtained $\nu=1.4 \pm 0.3$ is compatible with the value found in numerical simulations of the true random 3D Anderson model [11,12]. We emphasize that there are no adjustable parameters in our procedure; all parameters are determined using the atoms themselves as probes.

VI. UNIVERSALITY OF THE ANDERSON TRANSITION

At this point, a reasonable question is: Does the quasiperiodic kicked rotor exhibit the same critical phenomena, i.e., belong to the same (orthogonal) universality class [64]—as the true 3D-Anderson model? Can this simple three-frequency dynamical system exactly mimic the critical behavior of 3D disordered electronic conductors? In this section, we show that the answer is positive: the *three-frequency quasiperiodic kicked rotor* and the *true 3D-Anderson model* belong to the *same universality class*. This is a strong claim that relies on a very precise determination of the critical ex-

ponent ν . The accuracy of this determination is comparable to that obtained in the most sophisticated numerical studies of the 3D Anderson model [12,72]. Within numerical uncertainties, the critical exponent is found to be universal and identical to the one found for the 3D-Anderson model [12]. The technical details of the calculation have already been reported in [73]. We here just discuss the essential ingredients proving universality.

A. Precise estimate of the critical exponent

Reliably distinguishing the different universality classes of the Anderson transition requires a very precise determination of the critical exponent; for instance, the value $\nu = 1.43 \pm 0.04$ for the unitary symmetry class is close to the one for the orthogonal symmetry class [74] $\nu = 1.57 \pm 0.02$.

The main uncertainty in our experimental determination of the critical exponent is due to statistical errors on Π_0 and to the limited duration of the experiment. However, numerical simulations are not limited to 150 kicks but can be ran for several thousands of kicks, and statistical uncertainties on $\langle p^2 \rangle$ can be sharply reduced by averaging over initial conditions. The numerical inaccuracy in the finite-time scaling determination of ν from the numerical data is thus mainly due to the procedure failing to reproduce the singular behavior of the scaling function at the critical point.

How can one improve the accuracy on the determination of the critical exponent ν ? This can be achieved by fitting directly the raw data $\ln \Lambda(K, t)$. The starting point of our analysis is the behavior of the scaling function $\mathcal{F} \equiv \ln F$ in the vicinity of the critical point,

$$\ln \Lambda = \ln F[(K - K_c)t^{1/3\nu}] = \mathcal{F}[(K - K_c)t^{1/3\nu}]. \quad (49)$$

As $\ln \Lambda(K, t)$ is an analytical function for *finite* t (Fig. 11), the scaling function \mathcal{F} can be expanded around K_c ,

$$\ln \Lambda(t) \simeq \ln \Lambda_c + (K - K_c)t^{1/3\nu} \mathcal{F}_1 + \dots, \quad (50)$$

where $\ln \Lambda_c \equiv \mathcal{F}[0]$ and $\mathcal{F}_1 = d\mathcal{F}(x)/dx|_{x=0}$.

A remarkable feature of Eq. (50) is that when $\ln \Lambda$ is plotted against K , the curves for different times t should intersect at a common point $(K_c, \ln \Lambda_c)$, and this crossing indicates the occurrence of the metal-insulator transition. This is clearly visible in Fig. 13. Another interesting feature of Eq. (50) is that the critical exponent ν can be determined from the slope of $\ln \Lambda$ at K_c

$$(\ln \Lambda)'(K_c, t) \equiv \left. \frac{\partial \ln \Lambda(K, t)}{\partial K} \right|_{K=K_c} \propto t^{1/3\nu}. \quad (51)$$

This is the simplest procedure to evaluate the critical exponent: $(\ln \Lambda)'(K_c, t)$ is evaluated by linear regression of $\ln \Lambda$ vs K in a small interval near K_c , giving an exponent $\nu \simeq 1.61 \pm 0.10$ (see Fig. 14). The linear regime has nevertheless very small size $(K - K_c)t^{1/3\nu} \ll 1$, and neglecting nonlinear corrections leads to systematic errors on the estimation of ν . This is why the error ± 0.1 refers to systematic errors and not to the uncertainty on the fitting parameters, which is much smaller as easily seen in Fig. 14.

In practice, there are small systematic deviations from Eq. (50). Such deviations can have different sources: (i) the pres-

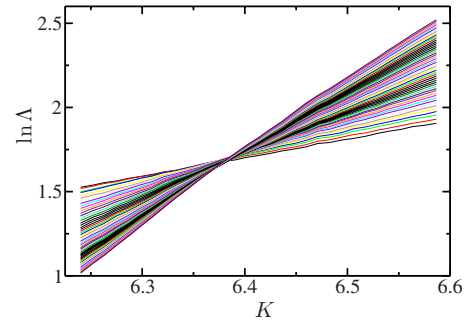


FIG. 13. (Color online) Dynamics of the quasiperiodic kicked rotor in the vicinity of the critical regime. The rescaled quantity $\ln \Lambda(K, t)$ vs K is plotted from $t=30$ to $t=40\,000$. All curves intersect, to a very good approximation, at a single point $(K_c \simeq 6.4, \ln \Lambda_c \simeq 1.6)$. This multiple crossing indicates the occurrence of the metal-insulator transition. Small deviations from crossing are due to the existence of an irrelevant scaling parameter at finite time and residual correlations in the disordered potential (see text). K and ϵ are swept along the straight line drawn in Fig. 6. Parameters are $k=2.85$, $\omega_2=2\pi\sqrt{5}$, and $\omega_3=2\pi\sqrt{13}$.

ence of an irrelevant scaling variable, that is when, in addition to $(K - K_c)t^{1/3\nu}$, $(\ln \Lambda)$ depends also on another scaling variable which vanishes in the limit $t \rightarrow \infty$, but still plays a role at short time; (ii) nonlinear dependence of the scaling variables in the stochasticity parameter K ; (iii) resonances due to the periods being well approximated by a ratio of small integers.

The latter one is specific to our three-frequency dynamical system, but the former two also play an important role in the standard Anderson model [11,12]. These small corrections can be taken into account—following the method devised in [12] for the Anderson model—by slightly modifying the basic scaling law [Eq. (45)] in two ways: introduce a nonlinear of the argument of the \mathcal{F} function with $K - K_c$ in Eq. (49), on one hand, and allow to subtract irrelevant scaling corrections to $(\ln \Lambda)$, on the other hand. To minimize the effect of resonances, we only retain data for sufficiently long times and average over different initial conditions, i.e., different quasimomenta β and phases φ_2 and φ_3 .

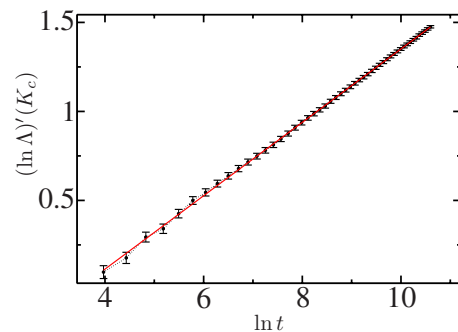


FIG. 14. (Color online) Linear regression of $(\ln \Lambda)'(K_c, t)$ [Eq. (51)] vs $\ln t$ for $t=30$ to $t=40\,000$ permits to extract the critical exponent ν from the slope $1/3\nu$, which is $\nu=1.61$. It is difficult to assess the uncertainty associated with this measurement as it depends crucially on the interval of K , where the behavior of $\ln \Lambda$ vs K can be assumed to be “linear.” The parameters are the same as in Fig. 13.

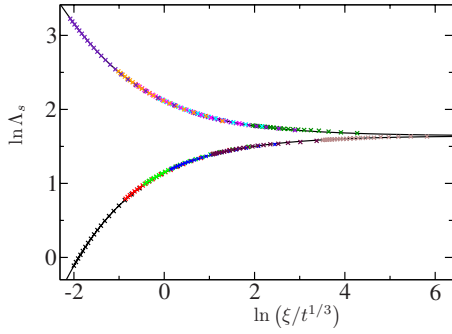


FIG. 15. (Color online) $\ln \Lambda_s$, after subtraction of corrections due to the irrelevant scaling variable, plotted versus $\ln(\xi/t^{1/3})$ and the scaling function deduced from the model (black curve). The parameters are that of the set \mathcal{D} (see Table I). The best-fit estimates of the critical stochasticity and the critical exponent are in this case: $K_c = 8.09 \pm 0.01$, $\ln \Lambda_c = 1.64 \pm 0.03$, and $\nu = 1.59 \pm 0.01$.

We computed $\ln \Lambda$ for times up to $t = 10^6$ kicks with an accuracy of 0.15%, for which more than 1000 initial conditions are required. We analyze data over the full range of times $t \in [10^3, 10^6]$. The best fit is determined by minimizing the deviation

$$\chi^2 = \sum_{K,t} \left[\frac{\ln \Lambda(K,t) - \mathcal{F}(K,t)}{\sigma(K,t)} \right]^2, \quad (52)$$

where $\sigma(K,t)$ is the numerical uncertainty (one standard deviation) of the computed quantities $\ln \Lambda(K,t)$.

In Fig. 15, we plot the scaling function corrected from the irrelevant scaling variable, as a function of $\xi(K)/t^{1/3}$. All data collapse almost perfectly on the scaling function deduced from the model.

Since the measurement errors in the data introduce some uncertainty in the determination of the fitted parameters, the confidence intervals for the fitted parameters were estimated using the bootstrap method, which yields Monte Carlo estimates of the errors in the fitted parameters [75]. The fitted parameters presented below are given with the corresponding 68.2% confidence intervals (standard errors).

B. Universality of the critical exponent

A key property of the Anderson transition is that the critical behavior can be described [74,76] in a framework of universality classes. This means that the critical behavior should not be sensitive of the microscopic details but should

depend only on the underlying symmetries of the system (e.g., time-reversal symmetry). Irrelevant parameters become negligible for sufficiently long times/large system size, whereas the relevant parameter behavior is universal. This brings the universality of the critical exponents. When considering a system with pseudorandom disorder, such as the quasiperiodic kicked rotor, one could ask whether the universality is broken or not due to correlations in the disorder potential. To answer the question, we changed some parameters that govern the microscopic details of the disorder potential of the quasiperiodic kicked rotor, namely, \tilde{k} , ω_2 , and ω_3 and the path along which we cross the transition.

The computer time required in those sophisticated numerical studies is very long. Therefore, we chose to restrict ourselves to the *detailed* study of only four different cases (see Table I).

The estimated critical parameters and their confidence intervals are given in Table II. A *typical* scaling function is drawn in Fig. 15.

The most important point to be drawn from Table II is that the estimates of the exponent ν for the four different sets are in almost perfect agreement with each other and with the estimate of ν based on numerical studies of the true random Anderson model $\nu = 1.57 \pm 0.02$ of the orthogonal symmetry class [12]. Note also that in the case of the quasiperiodic kicked rotor, the critical stochasticity K_c and $\ln \Lambda_c$ depend on (i) the anisotropy governed by the parameter ε and (ii) \tilde{k} , ω_2 , and ω_3 . The dependence (i) of the critical disorder and critical $\ln \Lambda$ on anisotropy is a typical feature of the Anderson transition in anisotropic solids [49–51]. The quasiperiodic kicked rotor may indeed be seen to correspond to a model of random chains (coupled by terms scaling like ε in the two transverse directions) considered in [50] [see Eq. (33)]. The dependence (ii) follows from the relation between the initial “classical” diffusion constant (see Sec. II) and the parameters \tilde{k} , ω_2 , and ω_3 . Such a dependence was observed both numerically and experimentally for the standard kicked rotor [77,78] and was accounted for in terms of correlations between the kicks by Shepelyansky in his early work [77].

The Anderson transition with the quasiperiodic kicked rotor is a robust feature: we observed that, for certain mutually incommensurate triplets $(\tilde{k}, \omega_2, \omega_3)$, systematic deviations to scaling (such as resonances) can occur for intermediate times, but eventually vanish.

VII. CONCLUSION

We discussed in detail, in the present work, the unambiguous evidence of the Anderson transition in 3D with atomic

TABLE I. The four sets of parameters considered: \tilde{k} , ω_2 and ω_3 control the microscopic details of the disorder, while ε drives the anisotropy of the hopping amplitudes. $\eta = 1.324\,717\dots$ is the silver number, i.e., the real root of the equation $\eta^3 - \eta - 1 = 0$ (see [73]).

	\tilde{k}	ω_2	ω_3	K	ε
\mathcal{A}	2.85	$2\pi\sqrt{5}$	$2\pi\sqrt{13}$	$6.24 \rightarrow 6.58$	$0.413 \rightarrow 0.462$
\mathcal{B}	2.85	$2\pi\sqrt{7}$	$2\pi\sqrt{17}$	$5.49 \rightarrow 5.57$	$0.499 \rightarrow 0.514$
\mathcal{C}	2.2516	$1/\eta$	$1/\eta^2$	$4.98 \rightarrow 5.05$	$0.423 \rightarrow 0.436$
\mathcal{D}	3.5399	k^-/η	k^-/η^2	$7.9 \rightarrow 8.3$	$0.425 \rightarrow 0.485$

TABLE II. Best-fit estimates of the critical parameters K_c and $\ln \Lambda_c$, the critical exponent ν together with their uncertainty (one standard deviation). ν is expected to be universal, whereas $\ln \Lambda_c$ and K_c do depend on anisotropy [50] and k , ω_2 , and ω_3 . y is strictly positive and should not necessarily be universal.

	K_c	$\ln \Lambda_c$	ν	y
\mathcal{A}	6.36 ± 0.02	1.60 ± 0.04	1.58 ± 0.01	0.71 ± 0.28
\mathcal{B}	5.53 ± 0.03	1.08 ± 0.09	1.60 ± 0.03	0.33 ± 0.30
\mathcal{C}	5.00 ± 0.03	1.19 ± 0.15	1.60 ± 0.02	0.23 ± 0.29
\mathcal{D}	8.09 ± 0.01	1.64 ± 0.03	1.59 ± 0.01	0.43 ± 0.23

matter waves with atomic matter waves by realizing experimentally a quasiperiodic kicked rotor. This allowed us to put into evidence the existence of the transition and to measure its critical exponent thanks to a finite-time scaling procedure. Our numerical result $\nu=1.59 \pm 0.01$ is in perfect agreement with the current value for the Anderson model and is compatible with our experimental determination 1.4 ± 0.3 . We have also shown that the quasiperiodic kicked rotor exhibits the same critical phenomena as the truly random Anderson model and, therefore, that both systems belong to the same (orthogonal) universality class.

These results are particularly relevant since they show that it is possible to explore a system like the Anderson

model that played an important role in many areas of physics but resisted thorough experimental investigations. One can guess that this kind of analogy will be extended to other models in the near future, as evidenced by the work of Wang and Gong [79] concerning the analogy of a quantum kicked rotor and the Harper model. This shall open new and exciting tracks in cold-atom physics. These analog models can even prove more flexible and more powerful than the original ones, as, for example, our Anderson-equivalent system can very easily be extended to higher dimensions by introducing additional incommensurate frequencies. Intermediate situations, like a 2D kicked rotor with two or three incommensurate frequencies, might be a convenient solution from the experimental point of view. This can hardly be done in condensed-matter systems or even in the ultracold atom realization of the 1D Anderson model [22]. The theoretical study of quantum phase transitions in high dimensions will most probably be boosted as experimental results become available. We are presently working in this direction. Numerical and experimental determinations of the critical exponents in four dimensions seem feasible.

ACKNOWLEDGMENT

The authors are pleased to acknowledge H. Lignier for fruitful discussions.

-
- [1] F. Bloch, *Z. Phys.* **52**, 555 (1928).
[2] C. Zener, *Proc. R. Soc. London, Ser. A* **145**, 523 (1934).
[3] P. W. Anderson, *Phys. Rev.* **109**, 1492 (1958).
[4] D. J. Thouless, *Phys. Rep.* **13**, 93 (1974).
[5] J. T. Edwards and D. J. Thouless, *J. Phys. C* **5**, 807 (1972).
[6] F. Wegner, *Z. Phys.* **B25**, 327 (1976).
[7] R. Landauer, *Philos. Mag.* **21**, 863 (1970).
[8] E. Abrahams, P. W. Anderson, D. C. Licciardello, and T. V. Ramakrishnan, *Phys. Rev. Lett.* **42**, 673 (1979).
[9] A. MacKinnon and B. Kramer, *Phys. Rev. Lett.* **47**, 1546 (1981).
[10] J. L. Pichard and G. Sarma, *J. Phys. C* **14**, L127 (1981).
[11] A. Mackinnon, *J. Phys. C: Condens. Matter* **6**, 2511 (1994).
[12] K. Slevin and T. Ohtsuki, *Phys. Rev. Lett.* **82**, 382 (1999).
[13] D. Vollhardt and P. Wölfle, *Phys. Rev. Lett.* **48**, 699 (1982).
[14] P. A. Lee and T. V. Ramakrishnan, *Rev. Mod. Phys.* **57**, 287 (1985).
[15] D. M. Basko, I. L. Aleiner, and B. L. Altshuler, *Ann. Phys.* **321**, 1126 (2006).
[16] B. Kramer and A. Mackinnon, *Rep. Prog. Phys.* **56**, 1469 (1993).
[17] M. Störzer, P. Gross, C. M. Aegerter, and G. Maret, *Phys. Rev. Lett.* **96**, 063904 (2006).
[18] T. Schwartz, G. Bartal, S. Fishman, and B. Segev, *Nature (London)* **446**, 52 (2007).
[19] C. A. Condat and T. R. Kirkpatrick, *Phys. Rev. B* **36**, 6782 (1987).
[20] I. S. Graham, L. Piché, and M. Grant, *Phys. Rev. Lett.* **64**, 3135 (1990).
[21] H. Hu, A. Strybulevych, J. H. Page, S. E. Skipetrov, and B. A. van Tiggelen, *Nature Phys.* **4**, 945 (2008).
[22] J. Billy, V. Josse, Z. Zuo, A. Bernard, B. Hambrecht, P. Lugan, D. Clément, L. Sanchez-Palencia, P. Bouyer, and A. Aspect, *Nature (London)* **453**, 891 (2008).
[23] B. V. Chirikov, *Phys. Rep.* **52**, 263 (1979).
[24] G. Casati, B. V. Chirikov, J. Ford, and F. M. Izrailev, *Stochastic Behavior of a Quantum Pendulum Under Periodic Perturbation* (Springer-Verlag, Berlin, 1979), Vol. 93, pp. 334–352.
[25] D. R. Grempel, R. E. Prange, and S. Fishman, *Phys. Rev. A* **29**, 1639 (1984).
[26] G. Casati, I. Guarneri, and D. L. Shepelyansky, *Phys. Rev. Lett.* **62**, 345 (1989).
[27] F. L. Moore, J. C. Robinson, C. F. Bharucha, B. Sundaram, and M. G. Raizen, *Phys. Rev. Lett.* **75**, 4598 (1995).
[28] J. Chabé, G. Lemarié, B. Grémaud, D. Delande, P. Szriftgiser, and J. C. Garreau, *Phys. Rev. Lett.* **101**, 255702 (2008).
[29] F. M. Izrailev, *Phys. Rep.* **196**, 299 (1990).
[30] D. L. Shepelyansky, *Phys. Rev. Lett.* **56**, 677 (1986).
[31] When the quasimomentum is taken into account, m should simply be replaced by $m+\beta$, leaving the conclusions unaffected.
[32] $W(\theta)$ is singular for $K/k > \pi$ and the behavior of W_r is complicated. However, this nonphysical singularity can be avoided by a mapping on a different tight-binding model [30].
[33] H. Lignier, J. C. Garreau, P. Szriftgiser, and D. Delande, *Europhys. Lett.* **69**, 327 (2005).

- [34] Y. V. Fyodorov and A. D. Mirlin, Phys. Rev. Lett. **67**, 2405 (1991).
- [35] K. Efetov, *Supersymmetry in Disorder and Chaos* (Cambridge University Press, Cambridge, UK, 1997).
- [36] A. Altland and M. R. Zirnbauer, Phys. Rev. Lett. **77**, 4536 (1996).
- [37] D. Vollhardt and P. Wölfle, Phys. Rev. B **22**, 4666 (1980).
- [38] A. Altland, Phys. Rev. Lett. **71**, 69 (1993).
- [39] E. Doron and S. Fishman, Phys. Rev. Lett. **60**, 867 (1988).
- [40] J. Wang and A. M. García-García, Phys. Rev. E **79**, 036206 (2009).
- [41] D. L. Shepelyansky, Physica D **8**, 208 (1983).
- [42] O. I. Lobkis and R. L. Weaver, Phys. Rev. E **71**, 011112 (2005).
- [43] R. Scharf, J. Phys. A **22**, 4223 (1989).
- [44] R. Blümel and U. Smilansky, Phys. Rev. Lett. **69**, 217 (1992).
- [45] F. Haake, *Quantum Signatures of Chaos*, 2nd ed. (Springer-Verlag, Berlin, 2001).
- [46] H. J. Stöckmann, *Quantum Chaos: An Introduction* (Cambridge University Press, Cambridge, UK, 1999).
- [47] D. M. Basko, M. A. Skvortsov, and V. E. Kravtsov, Phys. Rev. Lett. **90**, 096801 (2003).
- [48] F. Borgonovi and D. L. Shepelyansky, Physica D **109**, 24 (1997).
- [49] Q. Li, C. M. Soukoulis, E. N. Economou, and G. S. Grest, Phys. Rev. B **40**, 2825 (1989).
- [50] N. A. Panagiotides, S. N. Evangelou, and G. Theodorou, Phys. Rev. B **49**, 14122 (1994).
- [51] I. Zambetaki, Q. Li, E. N. Economou, and C. M. Soukoulis, Phys. Rev. Lett. **76**, 3614 (1996).
- [52] J. Ringot, Y. Lecoq, J. C. Garreau, and P. Szriftgiser, Eur. Phys. J. D **7**, 285 (1999).
- [53] J. Ringot, P. Szriftgiser, and J. C. Garreau, Phys. Rev. A **65**, 013403 (2001).
- [54] P. Szriftgiser, H. Lignier, J. Ringot, J. C. Garreau, and D. Delande, Commun. Nonlinear Sci. Numer. Simul. **8**, 301 (2003).
- [55] J. Chabé, H. Lignier, P. Szriftgiser, and J. C. Garreau, Opt. Commun. **274**, 254 (2007).
- [56] J. Ringot, P. Szriftgiser, J. C. Garreau, and D. Delande, Phys. Rev. Lett. **85**, 2741 (2000).
- [57] P. Szriftgiser, J. Ringot, D. Delande, and J. C. Garreau, Phys. Rev. Lett. **89**, 224101 (2002).
- [58] H. Lignier, J. Chabé, D. Delande, J. C. Garreau, and P. Szriftgiser, Phys. Rev. Lett. **95**, 234101 (2005).
- [59] J. Chabé, H. Lignier, H. Cavalcante, D. Delande, P. Szriftgiser, and J. C. Garreau, Phys. Rev. Lett. **97**, 264101 (2006).
- [60] W. H. Zurek, Rev. Mod. Phys. **75**, 715 (2003).
- [61] M. Janssen, Phys. Rep. **295**, 1 (1998).
- [62] G. Lemarié *et al.* (unpublished).
- [63] M. G. Raizen, F. L. Moore, J. C. Robinson, C. F. Bharucha, and B. Sundaram, J. Eur. Opt. Soc. Rapid Publ. **8**, 687 (1996).
- [64] F. Evers and A. D. Mirlin, Rev. Mod. Phys. **80**, 1355 (2008).
- [65] G. Lemarié *et al.* (unpublished).
- [66] D. Stauffer and A. Aharony, *Introduction to Percolation Theory*, 2nd ed. (Taylor and Francis, London, 1994).
- [67] T. Ohtsuki and T. Kawarabayashi, J. Phys. Soc. Jpn. **66**, 314 (1997).
- [68] A. D. Mirlin and Y. V. Fyodorov, Phys. Rev. Lett. **72**, 526 (1994).
- [69] A. MacKinnon and B. Kramer, Z. Phys. B **53**, 1 (1983).
- [70] A. M. García-García, Phys. Rev. Lett. **100**, 076404 (2008).
- [71] B. Shapiro and E. Abrahams, Phys. Rev. B **24**, 4889 (1981).
- [72] F. Milde, R. Römer, M. Schreiber, and V. Uski, Eur. Phys. J. B **15**, 685 (2000).
- [73] G. Lemarié, B. Grémaud, and D. Delande, EPL **87**, 37007 (2009).
- [74] K. Slevin and T. Ohtsuki, Phys. Rev. Lett. **78**, 4083 (1997).
- [75] W. H. Press, S. A. Teukolsky, W. T. Vetterling, and B. P. Flannery, *Numerical Recipes in Fortran: The Art of Scientific Computing*, 2nd ed. (Cambridge University Press, Cambridge, UK, 1992).
- [76] K. B. Efetov, Adv. Phys. **32**, 53 (1983).
- [77] D. L. Shepelyansky, Physica D **28**, 103 (1987).
- [78] D. A. Steck, V. Milner, W. H. Oskay, and M. G. Raizen, Phys. Rev. E **62**, 3461 (2000).
- [79] J. Wang and J. Gong, Phys. Rev. A **77**, 031405(R) (2008).